

Characteristics of two-dimensional vortex dynamics from XY -type models with Ginzburg-Landau dynamics

Anna Jonsson and Petter Minnhagen

Department of Theoretical Physics, Umeå University, 901 87 Umeå, Sweden

(Received 7 May 1996)

The characteristic features of vortex dynamics corresponding to two-dimensional XY -type models with Ginzburg-Landau dynamics are extracted from simulations. The cases covered are with and without frustration, as well as above and below the Kosterlitz-Thouless transition. Most of the results are very well described by a phenomenological response function. The dependence of the characteristic frequency for this response function on the vortex density, frustration, correlation length, and temperature is obtained. A critical behavior for vortex dynamics at the Kosterlitz-Thouless transition is suggested by the simulations. The agreements with experiments and other simulations are discussed. [S0163-1829(97)04514-1]

I. INTRODUCTION

The aim of the present investigation is to extract characteristic features for two-dimensional (2D) vortex dynamics from simulations of 2D XY -type models. Our general motivation for this investigation is that some of these characteristic features of 2D vortex dynamics should be quite generic for a large class of systems. The systems we in particular have in mind are 2D superconductors and 2D Josephson-junction coupled arrays. For these types of systems there exist experimental data. Thus our hope is to get some further insight into the characteristic features of 2D vortex fluctuations for these real systems by studying vortex dynamics for XY -type models.

The 2D XY model undergoes a Kosterlitz-Thouless transition driven by vortex fluctuations just like the 2D superconductors and the 2D Josephson coupled arrays.^{1,2} This means that in a region around the transition the behavior is dominated by the thermally created vortices. We also investigate the case when, in addition to these thermally created vortices, additional vortices are introduced by frustrating the model. This would, e.g., correspond to a 2D Josephson coupled array in a perpendicular magnetic field. There exists high precision measurements for these type of Josephson-junction arrays in small magnetic fields to compare with.³ This comparison suggests to us that the simulations and measurements reflect precisely the same generic vortex dynamics. The simulations also show that the flux noise approximately goes like $1/\omega$ over a limited region which increases in decades as the Kosterlitz-Thouless (KT) transition is approached from above. This feature is discussed in connection with flux noise measurements.^{4,5}

Dynamics can be introduced into the 2D XY -type models in several ways. In the present investigation we have for simplicity chosen a time-dependent Ginzburg-Landau (TDGL)-type dynamics.^{6,7} This makes it possible to converge the simulations much easier than for the XY model with resistively shunted junction (RSJ) dynamics.⁸ The underlying assumption is that the characteristic features of vortex dynamics are anyway rather insensitive to the precise choice of dynamics. Earlier comparisons between the XY

model with TDGL dynamics and experiments support this view⁷ as do recent comparisons with the 2D Coulomb gas model with Langevin dynamics.⁹

We have to a large extent chosen to analyze the simulation data in terms of the Minnhagen phenomenology (MP) response function^{2,7,9} which is given by Eqs. (15) and (16). This is convenient because the present simulations as well as experimental data for both 2D superconductors and 2D Josephson-junction arrays are very well described by the functional form of the MP response.^{2,3,5,10} Thus we suggest that the MP response function can be viewed as a characteristic feature of 2D vortex dynamics. Accordingly, we have to a large extent focused on how the characteristic frequency in the MP response function depends on temperature and frustration. However, there are also interesting deviations from the MP response which we will discuss.

The paper is organized as follows. In Sec. II we introduce the model, the dynamics, and describe how the simulations are done. Since we are interested in the vortex dynamics we have to extract the relevant vortex variables. How this is done is explained in Sec. III where we also introduce the 2D Coulomb gas variables; Coulomb gas temperature T^{CG} , particle density n , static dielectric function $\epsilon(k)$, screening length λ , and dielectric constant $\bar{\epsilon}$. In Sec. IV we present the 2D vortex dynamics results for the case with no frustration both below and above the KT transition. Relations between the MP characteristic frequency, the screening length, and the vortex density are obtained. Section V describes the corresponding result for the frustrated case. Relations between the MP characteristic frequency, the frustration, and the vortex density are found. Section VI focuses on small deviations from the MP response function. Section VII discusses the connection between the results found in the simulations and experiments. Finally, Sec. VIII contains some concluding remarks.

II. MODEL AND DYNAMICS

The 2D XY model is defined on a 2D square lattice where each lattice point i is associated with a phase angle θ_i . The lattice variables interact with a nearest-neighbor coupling

which in the absence of frustration is given by the Hamiltonian

$$H = \sum_{\langle ij \rangle} U(\phi_{ij} = \theta_i - \theta_j), \quad (1)$$

where

$$U(\phi) = 2J[1 - \cos^{2p}(\phi/2)]. \quad (2)$$

Here $\langle ij \rangle$ denotes sum over nearest-neighbor pairs and $-\pi < \phi < \pi$. $U(\phi)$ reduces for $p=1$ to the usual XY interaction $U(\phi) = J(1 - \cos\phi)$. The point of the generalization to Eq. (2) with $p > 1$ is that a larger value of p makes it easier to create vortices.¹¹ Consequently, the larger p the more thermally created vortex fluctuations and the more dominating becomes the vortex response. However, for p exceeding some maximum value (i.e., $p > p_{\max} \approx 6$) the phase transition of the model changes from KT type to first order.^{11,12} The main part of the results in the present paper is for $p=2$ which is well inside the KT transition region, yet is large enough to ensure substantial vortex fluctuations over a temperature region around the phase transition. We also make comparisons with the standard XY model corresponding to $p=1$.

We use periodic boundary conditions in the simulations and the results presented are for lattice sizes $L \times L$ where $L = 64, 96,$ and 128 . The lattice constant a is set to 1. The frustration is introduced into the model through a vector potential associated with each link A_{ij} so that the argument in the cosine of the Hamiltonian changes to $\phi_{ij} - A_{ij}$. In order to introduce the frustration ($f \geq 0$) we choose the vector potential for the links belonging to row m to be identical and equal to $A_{ij} = 2\pi m f$. The periodic boundary condition then constrains $2\pi L f$ to be a multiple of 2π .

The dynamics of the model is introduced through the Langevin equation^{6,7}

$$\frac{d\theta_i(t)}{dt} = -\Gamma \frac{\partial H}{\partial \theta_i} + \eta_i(t), \quad (3)$$

where Γ is a constant which determines the relaxation and $\eta_i(t)$ is a fluctuating noise associated with each lattice point such that

$$\langle \eta_i(t) \eta_j(t') \rangle = 2\Gamma T \delta_{ij} \delta(t-t'), \quad (4)$$

where T is the temperature (in energy units, Boltzmann's constant $k_B = 1$). We integrate Eq. (3) by discretizing time into small enough steps subject to a random noise defined by Eq. (4) at each time step. We use a two-valued random noise $\eta_i = \pm \sqrt{\Gamma T}$, which turns out to be an efficient choice for the present type of problem.¹³

The information about the vortex dynamics is extracted from the time correlation function $G(t)$ given by

$$G(t) \equiv \frac{1}{L^2} \langle F(t) F(0) \rangle, \quad (5)$$

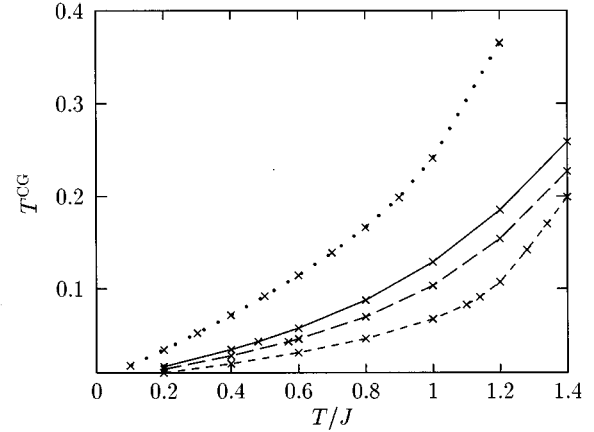


FIG. 1. Coulomb gas temperature T^{CG} as a function of T/J . The dotted curve corresponds to $p=1, f=0$. The short dashed, long dashed, and full curves correspond to $p=2$ and $f=0, f=1/16,$ and $f=1/8$, respectively.

where

$$F(t) \equiv \sum_{\langle ij \rangle_x} U'[\phi_{ij}(t) - A_{ij}], \quad (6)$$

where U' is the derivative and the sum is over all nearest-neighbor pair in one of the basic lattice directions (e.g., all pairs parallel to the x direction).

In order to translate the information from this time correlation function into vortex dynamics we also have to calculate some static correlation functions. How this translation is done and which static correlation functions are needed is explained in the next section.

III. COULOMB GAS ANALOGY

It is often convenient to discuss 2D vortices in terms of a Coulomb gas analogy. The vortices correspond to Coulomb gas charges which in two dimensions have a logarithmic interaction.² The Coulomb gas particles (or vortices) are associated with an effective dimensionless Coulomb gas temperature T^{CG} .² This effective temperature is for the XY model given by¹⁴

$$T^{\text{CG}} = \frac{T}{2\pi \langle U'' \rangle}, \quad (7)$$

where $\langle \rangle$ denote the thermal average. One may note that for a 2D superfluid the Coulomb gas temperature is given by $T^{\text{CG}} = T/[2\pi\rho_0(\hbar/m^*)^2]$, where ρ_0 is the bare (areal) superfluid density.² Consequently, the bare superfluid density corresponds to $\langle U'' \rangle$ in case of the XY model. T^{CG} for the XY model depends on U and thus on the value of p in Eq. (2). One also realizes that T^{CG} for the XY model depends on both T and the frustration f . Consequently, T^{CG} is a function of f for a fixed T . These features are illustrated in Fig. 1 which shows T^{CG} as a function of T/J for $p=1, f=0$ (dotted curve); $p=2, f=0$ (short dashed curve); $p=2, f=1/16$ (long dashed curve); and $p=2, f=1/8$ (full curve).

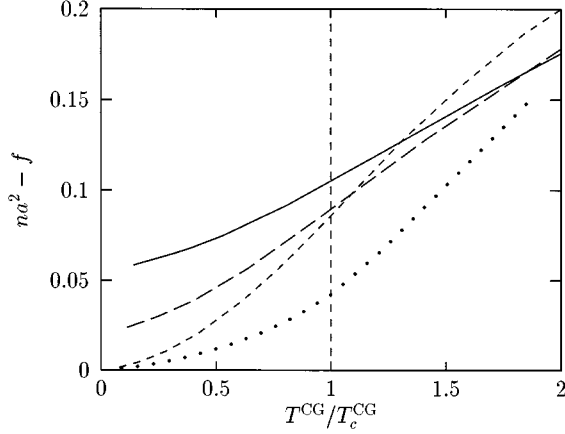


FIG. 2. Vortex density n as a function of $T_c^{\text{CG}}/T_c^{\text{CG}}$, where T_c^{CG} refers to $f=0$. The dotted curve corresponds to $p=1$ and $f=0$. The short dashed, long dashed, and full curves correspond to $p=2$ and $f=0$, $f=1/16$, and $f=1/8$, respectively. The vertical broken line denotes $T_c^{\text{CG}}/T_c^{\text{CG}}=1$.

The charge density associated with a fundamental square labeled by l in the quadratic lattice is given by the directed sum (corresponding to a line integral) over the four links ij making up the square^{14,15}

$$\Delta n(l) \equiv \frac{T_c^{\text{CG}}}{T} \left(\sum_{(ij) \in l} U' \right) - f. \quad (8)$$

The average particle density corresponds to

$$n = \frac{1}{L^2} \left\langle \sum_l |\Delta n(l)| \right\rangle. \quad (9)$$

Figure 2 shows the average density n as a function of $T_c^{\text{CG}}/T_c^{\text{CG}}$ for the same four cases as in Fig. 1 (T_c^{CG} is the KT transition temperature of the unfrustrated model). Figure 2 clearly demonstrates a main difference between the $p=1$ case (standard XY model) and the $p=2$ case; for a given f and $T_c^{\text{CG}}/T_c^{\text{CG}}$ the $p=2$ case contains more vortices than the $p=1$ case. As stated earlier this is the reason why we have chosen to focus on the $p=2$ case in order to extract the vortex properties. In Fig. 2 we have also plotted $n-f$ for the $p=2$ cases with frustration $f=1/16$ and $f=1/8$ where $n-f$ measures the density of vortex fluctuations. One notices that for a given p and a given T_c^{CG} below T_c^{CG} the density of vortex fluctuations increases with increasing f .

A fundamental quantity in the Coulomb-gas-vortex analysis is the dielectric function $\epsilon(\mathbf{k}, \omega)$ where \mathbf{k} is the wave vector and ω is the frequency. The static dielectric function $\epsilon(\mathbf{k}, 0)$ is in the unfrustrated case related to the XY model as follows.^{14,7} Define

$$F_m \equiv \sum_{(ij) \in m} U', \quad (10)$$

where m labels a row of the lattice and the sum is over all links making up this row. Next we define the one-dimensional Fourier transform $\hat{F}(k) = \sum_m F_m e^{ikm}$. The connection is then

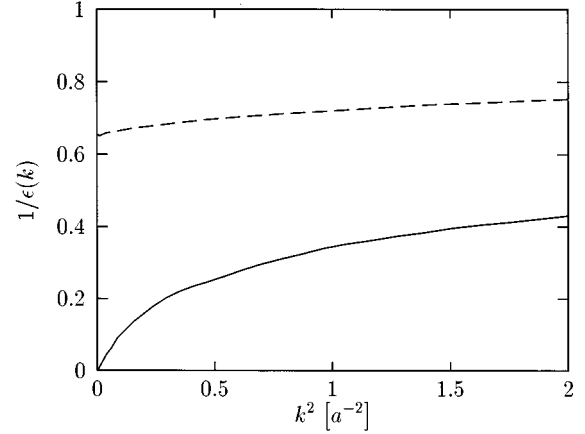


FIG. 3. $1/\epsilon(k)$ as a function of k^2 . The full and dashed curves correspond to $1/\epsilon(k)$ for a fixed temperature T_c^{CG} above and below T_c^{CG} , respectively.

$$\frac{1}{\epsilon(k, 0)} = 1 - \frac{2\pi T_c^{\text{CG}}}{T^2 L^2} \langle |\hat{F}(k)|^2 \rangle. \quad (11)$$

Figure 3 shows $1/\epsilon(k)$ obtained in this way. The full curve is for a fixed T_c^{CG} above the KT transition. In this case $1/\epsilon(k)$ goes to zero as $k \rightarrow 0$. The broken curve is for a fixed T_c^{CG} below the KT transition in which case $1/\epsilon(k)$ goes to a constant as $k \rightarrow 0$.

Below the KT critical temperature T_c^{CG} we will in the following only need the value $1/\epsilon(k=0)$. However, above T_c^{CG} we will in the unfrustrated case use the k dependence of $1/\epsilon(k)$ in order to extract the screening length λ as well as the dielectric constant $\tilde{\epsilon}$.² Basically we make use of the relation

$$\frac{1}{\epsilon(k)} = \frac{1}{\tilde{\epsilon}} \frac{k^2}{k^2 + \lambda^{-2}} \quad (12)$$

which is expected to be valid in the limit of small k .² In the present square lattice case this relation can be somewhat improved by replacing k^2 with $4\sin^2(k/2)$.¹⁴ The practical procedure we use is to plot $\epsilon(k)\sin^2(k/2)$ as a function of $\sin^2(k/2)$ and determine the best straight line through the data for small k . Figures 4(a) and 4(b) show λ^{-2} and $\tilde{\epsilon}$ determined in this way for the $p=2$ case. Note that λ in Fig. 4(a) diverges at the KT critical temperature T_c^{CG} where we determine T_c^{CG} from the KT critical condition $\tilde{\epsilon}T_c^{\text{CG}} = 1/4$. As seen from Eq. (12) we have $\tilde{\epsilon} = \epsilon(k=0)$ below T_c^{CG} since $\lambda = \infty$ in the low-temperature phase. Figure 4(b) shows $\tilde{\epsilon}$ both below and above T_c^{CG} . The dielectric constant $\tilde{\epsilon}$ is expected to approach 1 for $T_c^{\text{CG}} \rightarrow 0$ and $T_c^{\text{CG}} \rightarrow \infty$. In between it is expected to be larger than 1 and have a maximum just above T_c^{CG} .² These expectations are consistent with the results in Fig. 4(b).

The vortex dynamics is described by the complex frequency dependent function $\epsilon(\omega) \equiv \epsilon(k=0, \omega)$. This function is given by⁷

$$\text{Re} \left[\frac{1}{\epsilon(\omega)} \right] = \frac{1}{\epsilon(0)} + \frac{2\pi\omega T_c^{\text{CG}}}{T^2} \int_0^\infty dt \sin\omega t G(t) \quad (13)$$

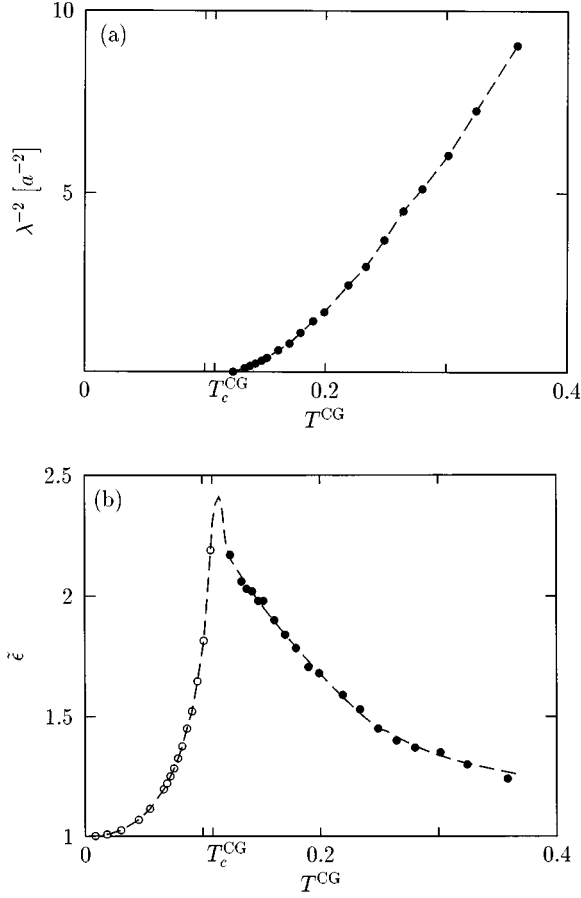


FIG. 4. (a) λ^{-2} as a function of Coulomb gas temperature. (b) The dielectric constant $\bar{\epsilon}$ as a function of Coulomb gas temperature. The dashed line is just a guide to the eye.

and

$$\text{Im}\left[\frac{1}{\epsilon(\omega)}\right] = -\frac{2\pi\omega T^{\text{CG}}}{T^2} \int_0^\infty dt \cos\omega t G(t), \quad (14)$$

where $G(t)$ was defined by Eqs. (5) and (6). Note that $1/\epsilon(0)$ is a real quantity. The response function $1/\epsilon(\omega)$ describes the dynamical response associated with the vortices.² We will in the following relate this dynamical response to other vortex quantities such as the vortex density n , the vortex screening length λ , and the effective vortex temperature T^{CG} .

IV. VORTEX DYNAMICS FOR THE UNFRUSTRATED CASE

In this section we analyze the dynamical vortex response contained in the function $1/\epsilon(\omega)$ for the XY model with $p=2$ and $f=0$. Figure 5 shows the real and imaginary parts of $1/\epsilon(\omega)$ as obtained from the simulations for a fixed temperature above [Fig. 5(a)] and below [Fig. 5(b)] the KT transition. We will in the following analysis use the fact that our simulated data is very well described by MP response function. The MP response function is given by²

$$\text{Re}\left[\frac{1}{\epsilon(\omega)} - \frac{1}{\epsilon(0)}\right] = \frac{1}{\bar{\epsilon}} \frac{\omega}{\omega + \omega_0} \quad (15)$$

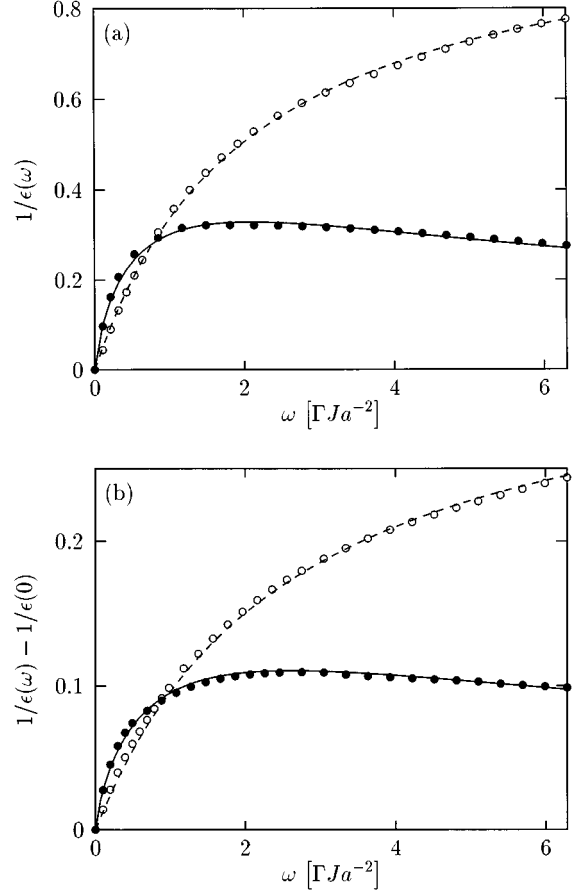


FIG. 5. The linear response function $1/\epsilon(\omega)$ as a function of ω for $p=2$ and $f=0$ for (a) fixed $T^{\text{CG}}(=0.23)$ above T_c^{CG} , (b) fixed $T^{\text{CG}}(=0.09)$ below T_c^{CG} . Open circles correspond to $\text{Re}[1/\epsilon(\omega)]$ and filled circles to $|\text{Im}[1/\epsilon(\omega)]|$. The full curves correspond to the imaginary part of the MP equation (16) and the broken curves correspond to the real part of the MP equation (15).

and

$$\text{Im}\left[\frac{1}{\epsilon(\omega)}\right] = -\frac{1}{\bar{\epsilon}} \frac{2}{\pi} \frac{\omega\omega_0 \ln\omega/\omega_0}{\omega^2 - \omega_0^2}. \quad (16)$$

Figure 5 demonstrates that Eqs. (15) and (16) give a very good representation of the simulated data *both* above [Fig. 5(a)] and below [Fig. 5(b)] the KT transition. In these fits the MP characteristic frequency ω_0 and $\bar{\epsilon}$ are adjustable parameters. The value of $\bar{\epsilon}$ obtained in this way is above T_c^{CG} somewhat closer to 1 compared to what is obtained directly from the static response function $\epsilon(k)$. However, the important point here is that the functional *form* given by Eqs. (15) and (16) is such a good description of the data for a rather wide temperature region around T_c^{CG} . This means that the characteristic frequency ω_0 is really the key quantity characterizing the dynamical response. Consequently, we focus on this quantity. A practical and unambiguous way of determining ω_0 is to note that according to Eqs. (15) and (16) the ratio $|\text{Im}[1/\epsilon(\omega)]|/\text{Re}[1/\epsilon(\omega) - 1/\epsilon(0)]$ is equal to $2/\pi$ precisely at ω_0 . This is sometimes referred to as the peak ratio because it occurs precisely at the maximum of $|\text{Im}[1/\epsilon(\omega)]|$. For convenience we have chosen to determine

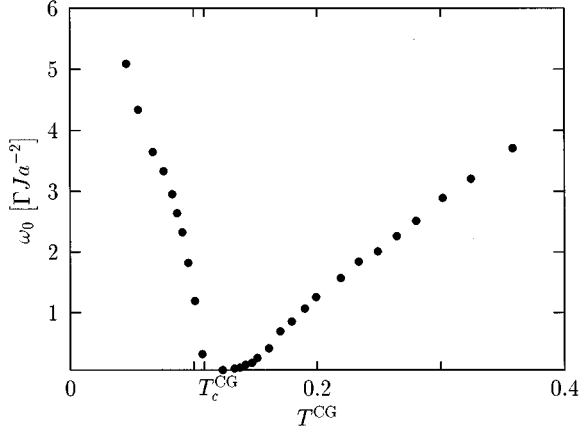


FIG. 6. The characteristic frequency ω_0 as a function of Coulomb gas temperature.

ω_0 from this $2/\pi$ ratio. Figure 6 shows the determined values of ω_0 as a function of T_c^{CG} . One notes that ω_0 vanishes as T_c^{CG} is approached both from above and from below.

The dynamical equation (3) has the natural time unit $a^2/\Gamma J$ or equivalently the frequency unit $\Gamma J/a^2$, where a is the lattice constant. It is then conceivable that the dimensionless ratio $\omega_0 a^2/\Gamma J$ is given by a dimensionless function of dimensionless combinations of variables related to the vortices. In the low-temperature phase one has $\lambda = \infty$ and the only natural length scale associated with the vortices (other than the lattice constant a related to the vortex core) is $n^{-1/2}$ which is related to the vortex density. Thus one may expect that

$$\omega_0 = \Gamma J n h(n a^2, T_c^{\text{CG}}), \quad (17)$$

where h is such a dimensionless function. Furthermore, let us suppose that the MP form given by Eqs. (15) and (16) describes a limiting behavior which contains no explicit dependence on the short distance scale a . This assumption implies the limit $n a^2 \rightarrow 0$. Thus according to Eq. (17) this assumption implies that ω_0 should be proportional to n , where the proportionality constant only depends on T_c^{CG} . Figure 7 demon-

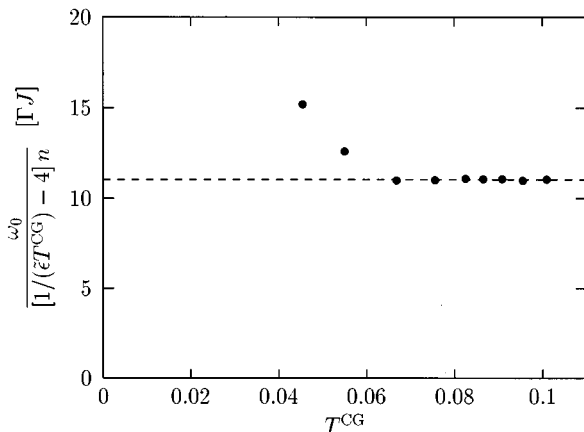


FIG. 7. The characteristic frequency ω_0 divided by $[1/(\tilde{\epsilon}T_c^{\text{CG}}) - 4]n$ as a function of Coulomb gas temperature below T_c^{CG} . The horizontal broken line is just a guide to the eye.

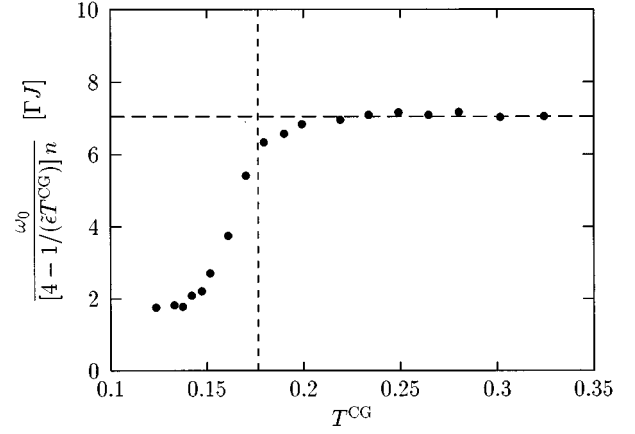


FIG. 8. The characteristic frequency ω_0 divided by $[4 - 1/(\tilde{\epsilon}T_c^{\text{CG}})]n$ as a function of Coulomb gas temperature above T_c^{CG} . The vertical dashed line denotes the temperature where $n\lambda^2 = 1/(2\pi)$. The horizontal broken line is just a guide to the eye.

strates that this hypothesis appears true. We have plotted ω_0 divided by $[1/(\tilde{\epsilon}T_c^{\text{CG}}) - 4]n$ as a function of T_c^{CG} . As seen in the figure the data points to very good approximation fall on a horizontal line. This implies that

$$\omega_0 \propto \left(\frac{1}{\tilde{\epsilon}T_c^{\text{CG}}} - 4 \right) n \quad (18)$$

over a rather large temperature region. This region apparently extends all the way up to the critical temperature T_c^{CG} . We may thus conclude that ω_0 is indeed proportional to n with a proportionality constant which is a function of only T_c^{CG} .

One may note that if Eq. (18) is precisely correct all the way up to T_c^{CG} (which is implied by Fig. 7 but which is of course impossible to verify by simulations on a finite lattice) then the implication is

$$\omega_0 \propto \sqrt{T_c^{\text{CG}} - T_c^{\text{CG}}} \quad (19)$$

as T_c^{CG} is approached from below. This follows from Eq. (18) because the KT critical behavior for $\tilde{\epsilon}(T_c^{\text{CG}})$ is given by $\tilde{\epsilon}(T_c^{\text{CG}}) - \tilde{\epsilon}(T_c^{\text{CG}}) \propto \sqrt{T_c^{\text{CG}} - T_c^{\text{CG}}}$ and $\tilde{\epsilon}(T_c^{\text{CG}})T_c^{\text{CG}} = 1/4$.²

We now turn to the high-temperature phase where λ is finite. This means that we now have two relevant length scales associated with the vortices besides the lattice constant a , i.e., λ and $n^{-1/2}$. The assumption that the MP form is associated with the limit $n a^2 \rightarrow 0$ in this case leads to the expectation

$$\omega_0 \propto n \tilde{h}(n\lambda^2, T_c^{\text{CG}}). \quad (20)$$

Consequently, we may expect different behavior in the two limits $n\lambda^2 \rightarrow 0$ and $n\lambda^2 \rightarrow \infty$. In Fig. 8 we have plotted ω_0 divided by $[4 - 1/(\tilde{\epsilon}T_c^{\text{CG}})]n$ versus T_c^{CG} . The data points in Fig. 8 to good approximation fall on a horizontal line for larger T_c^{CG} . However, as T_c^{CG} is approached from above there is a clear deviation. The vertical line in Fig. 8 denotes the temperature where $n\lambda^2 = 1/(2\pi)$. Thus the data imply that

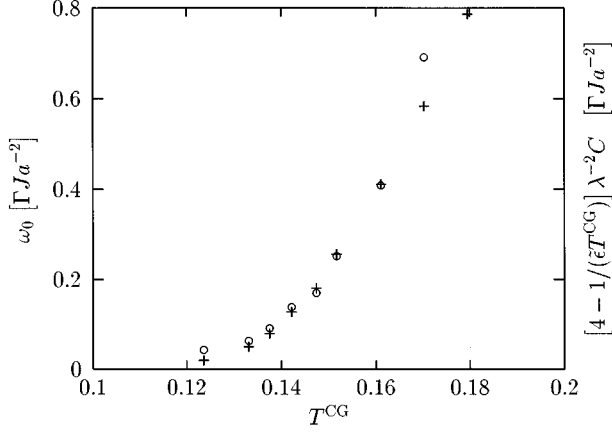


FIG. 9. The characteristic frequency ω_0 and $[4 - 1/(\bar{\epsilon}T^{\text{CG}})]\lambda^{-2}C$ as a function of Coulomb gas temperature. Open circles correspond to ω_0 and pluses to $[4 - 1/(\bar{\epsilon}T^{\text{CG}})]\lambda^{-2}C$. Here C is a fitting parameter. The figure shows that a constant C can be found which makes circles and pluses coincide in a region close to T_c .

$$\omega_0 \propto \left(4 - \frac{1}{\bar{\epsilon}T^{\text{CG}}}\right)n \quad (21)$$

for $n\lambda^2 \ll 1$. However, as T_c^{CG} is approached λ increases leading to a crossover to the region $n\lambda^2 \gg 1$ and Eq. (21) becomes invalid. In the original motivation for the MP form it was assumed that $\omega_0 \propto \lambda^{-2,2}$. Thus one may suspect that this is indeed the correct behavior closer to T_c^{CG} . This suggests that the dimensionless function \tilde{h} in Eq. (20) has the limit $\tilde{h} \propto 1/n\lambda^2$ as $n\lambda^2 \rightarrow \infty$. These expectations are put to test in Fig. 9 where we have plotted ω_0 versus T^{CG} and compare it to $[4 - 1/(\bar{\epsilon}T^{\text{CG}})]\lambda^{-2}C$. The figure demonstrates that the constant C can be chosen so that the two functions coalesce to good approximation. Consequently, the simulations suggest that

$$\omega_0 \propto \left(4 - \frac{1}{\bar{\epsilon}T^{\text{CG}}}\right)\lambda^{-2} \quad (22)$$

for $n\lambda^2 \gg 1$. If Eq. (22) holds all the way to T_c^{CG} then the KT critical behavior^{1,2} of λ and $\bar{\epsilon}$ translates into the critical behavior

$$\omega_0 \propto \sqrt{T^{\text{CG}} - T_c^{\text{CG}}} e^{-\text{const}/\sqrt{T^{\text{CG}} - T_c^{\text{CG}}}} \quad (23)$$

as T_c^{CG} is approached from above.

For the unfrustrated case we have thus identified three distinct behaviors, i.e., $\omega_0 \propto [1/(\bar{\epsilon}T^{\text{CG}}) - 4]n$ for $T^{\text{CG}} < T_c^{\text{CG}}$; $\omega_0 \propto [4 - 1/(\bar{\epsilon}T^{\text{CG}})]\lambda^{-2}$ for $T^{\text{CG}} > T_c^{\text{CG}}$ and $n\lambda^2 \gg 1$; $\omega_0 \propto [4 - 1/(\bar{\epsilon}T^{\text{CG}})]n$ for $T^{\text{CG}} > T_c^{\text{CG}}$ and $n\lambda^2 \ll 1$. This in turn implied the critical behaviors given by Eqs. (19) and (23). In the following section we investigate the frustrated case.

V. VORTEX DYNAMICS FOR THE FRUSTRATED CASE

Our analysis of the frustrated case follows the same lines as the unfrustrated case. We are only considering frustrations

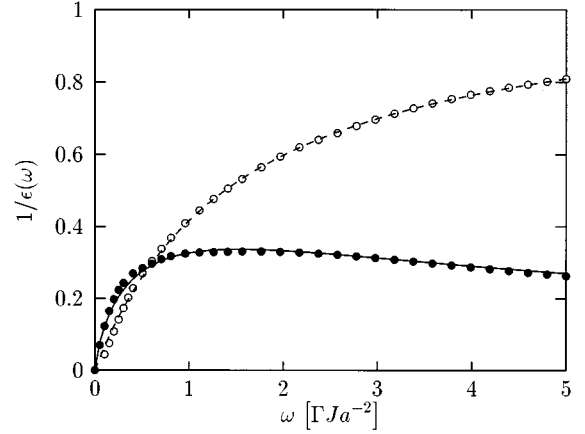


FIG. 10. The linear response function $1/\epsilon(\omega)$ as a function of ω for a temperature $T^{\text{CG}} (\approx 0.042)$ which is below $T_c^{\text{CG}}, p=2$ and $f=1/8$. The symbols are the same as in Fig. 5.

smaller than $1/2$, where $f=1/2$ corresponds to the fully frustrated case. The largest f included in our analysis is $f=1/8$. Just as in the unfrustrated case the simulations are very well described by the MP form of Eqs. (15) and (16). This is illustrated in Fig. 10 for the case $p=2$ and $f=1/8$. Consequently, we again focus on the MP characteristic frequency ω_0 . In Fig. 11 we have plotted ω_0/n versus T^{CG} . The figure includes data for $f=1/16, 1/12, 1/8$. All the data below T_c^{CG} coalesce to very good approximation on a horizontal line. Thus we conclude that for the frustrated case the relation is

$$\omega_0 \propto n, \quad (24)$$

where the proportionality constant is almost completely independent of T^{CG} over a wide region ($0.027 < T^{\text{CG}} < 0.11 \approx T_c^{\text{CG}}$, our determination gives $T_c^{\text{CG}} \approx 0.1085 \pm 0.0003$).

In the frustrated case we can estimate $\bar{\epsilon}$ by fitting the data to the MP form given by Eqs. (15) and (16). We then find that $\bar{\epsilon} \approx 1$ over a wide region. Consequently, both ω_0/n and

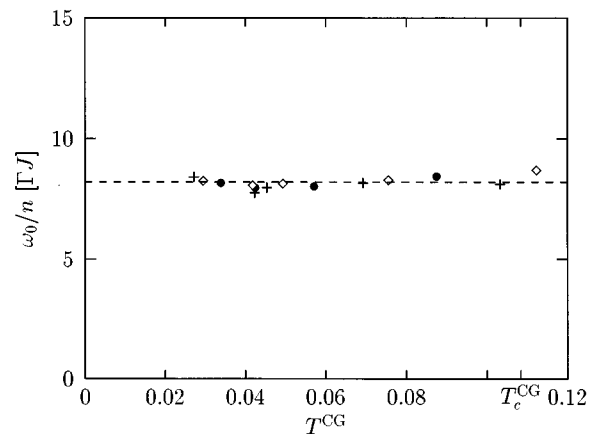


FIG. 11. ω_0/n as a function of T^{CG} for three different frustrations. Filled circles, open diamonds, and pluses correspond to $f=1/8, f=1/12, f=1/16$, respectively. The horizontal broken line is just a guide to the eye.

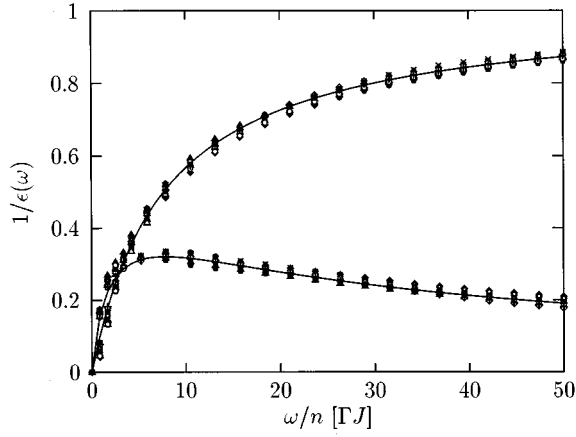


FIG. 12. $1/\epsilon(\omega)$ as a function of ω/n for three different frustrations and $T^{\text{CG}} \in [0.027, 0.11]$. Open diamonds, pluses, open squares, and crosses correspond to $f=1/8$, $T^{\text{CG}}=0.034$, 0.043 , 0.057 , and 0.087 , respectively. Open circles, open triangles, open pentagons, and filled diamonds correspond to $f=1/12$, $T^{\text{CG}}=0.029$, 0.049 , 0.076 , and 0.112 , respectively. Filled squares, filled triangles, filled circles, and filled pentagons correspond to $f=1/16$, $T^{\text{CG}}=0.027$, 0.045 , 0.069 , and 0.103 , respectively. The full curves correspond to the MP Eqs. (15) and (16).

$\tilde{\epsilon}$ are temperature independent over a wide range. This means that if $1/\epsilon(\omega)$ is plotted as a function of ω/n the data from different temperatures and different frustrations should collapse on a single curve. This data collapse is shown in Fig. 12. The data span the temperature interval $0.027 < T^{\text{CG}} < 0.11$ and the frustration interval $1/16 \leq f \leq 1/8$. The full curve is a fit to the MP form.

The vortex density n is to good approximation proportional to f over a wide temperature and frustration region. This proportionality is illustrated in Fig. 13. As seen in Fig. 13 the relation is to very good approximation $n = C_0 + Cf$, where C_0 is very small and C is rather independent of temperature, as shown in the inset of Fig. 13. This means that the data should also collapse on a single curve when plotted

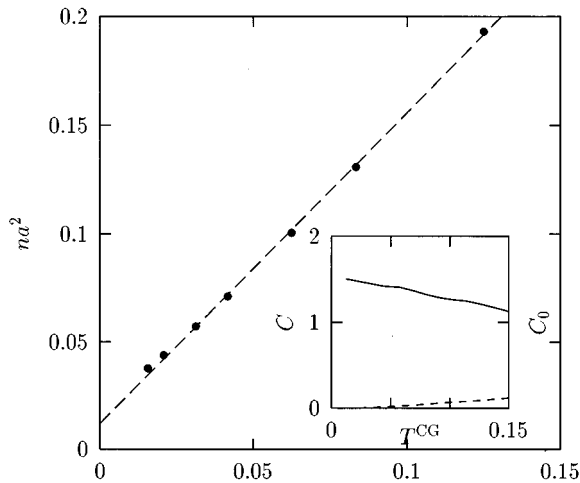


FIG. 13. The vortex density as a function of frustration, for fixed Coulomb gas temperature. The dashed line is a fit of the data points to $C_0 + Cf$. Inset shows C and C_0 as a function of T^{CG} . The full curve corresponds to C and the dashed curve to C_0 .

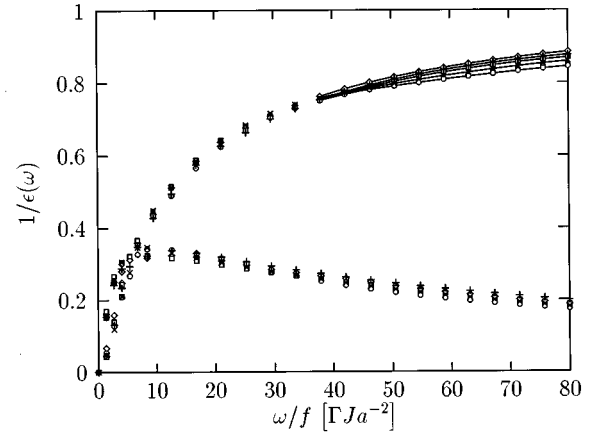


FIG. 14. $1/\epsilon(\omega)$ for fixed T/J , as a function of ω/f for five different frustrations. Open diamonds, pluses, open squares, crosses, and open circles correspond to $f=1/8$, $1/12$, $1/16$, $1/24$, and $f=1/32$, respectively. The full curves combining the points of $\text{Re}[1/\epsilon(\omega)]$ indicate a small but systematic spread for the large ω/f values.

versus ω/f provided the T^{CG} range is small enough for C to be constant. Suppose we choose a fixed T . The Coulomb gas temperature T^{CG} will then vary as a function of f (compare Fig. 1). However, there will always exist a range of frustrations over which the variation for T^{CG} for fixed T is small enough for C to be almost constant. Over such a range the data will again collapse on a single curve. This is illustrated in Fig. 14 where we have plotted $1/\epsilon(\omega)$ as a function of ω/f for a fixed T below T_c . However, it should be noted that ω/n is really the fundamental scaling variable in the sense that it causes a much wider range of data to collapse on a single curve. The ω/f scaling shown in Fig. 14 is in this sense just an approximation. On the other hand the ω/f scaling is more easily related to experiments, as will be discussed in Sec. VII.

VI. DEVIATIONS FROM THE MP RESPONSE

We will first discuss the $f=0$ case just above the KT transition. This region is hard to converge because of the

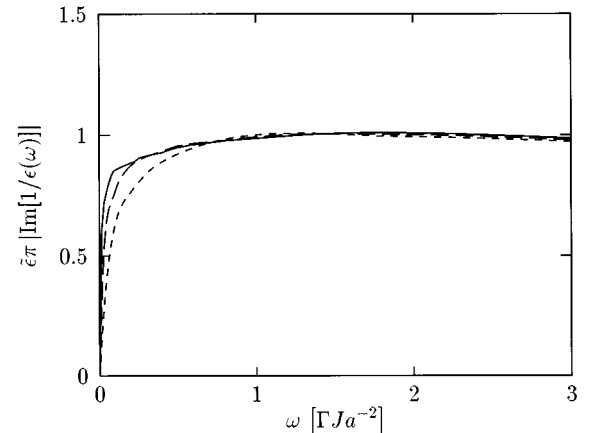


FIG. 15. $\tilde{\epsilon}\pi |\text{Im}[1/\epsilon(\omega)]|$ as a function of ω . The full, long dashed, and short dashed curves correspond to $T^{\text{CG}}=0.13$, 0.15 , and 0.17 , respectively.

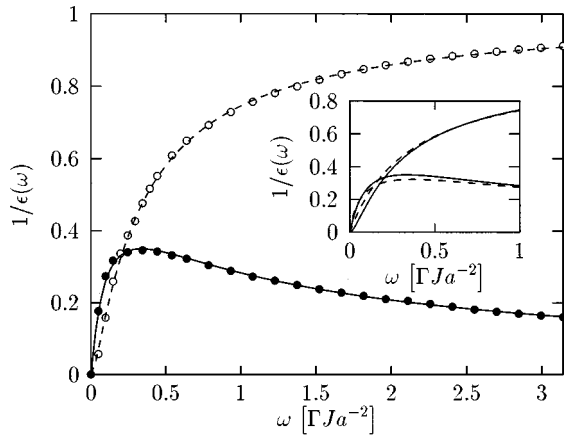


FIG. 16. The linear response function $1/\epsilon(\omega)$ as a function of ω for $p=1$ and $f=0$. The ratio between T_c^{CG} and T_c^{CG} is the same as in Fig. 5(a). Open circles correspond to $\text{Re}[1/\epsilon(\omega)]$ and filled circles to $|\text{Im}[1/\epsilon(\omega)]|$. The full curve corresponds to the imaginary part of the extended MP equation (26) and the broken curve correspond to the real part of the extended MP equation (25). The value $\sigma/\omega_0 \approx 0.4$ was obtained. Inset shows the difference between the extended MP equations and the pure MP response for this σ/ω_0 . The full curves correspond to Eqs. (25) and (26) and the dashed curves to the MP Eqs. (15) and (16).

critical slowing down as T_c^{CG} is approached. Nevertheless an interesting deviation from the MP form can be discerned in the data: the maximum of $|\text{Im}[1/\epsilon(\omega)]|$ becomes broad, as is seen in Fig. 15. This flat region extends typically from some small frequency ω_{\min} to some large frequency ω_{\max} . We empirically find $\omega_{\min} \approx \omega_0$ and that ω_{\max} is rather independent of T_c^{CG} , whereas $\omega_{\min} \approx \omega_0$ vanishes as T_c^{CG} goes to T_c^{CG} . Thus very close to the KT transition $|\text{Im}[1/\epsilon(\omega)]|$ becomes fairly constant over an extended interval $0 < \omega < \omega_{\max}$ (the simulations shown in Fig. 15 suggest that it varies by a factor less than 1.5 over the extended interval. However, the simulations cannot be converged in the region very close to the KT transition so in fact this factor might turn out to be smaller). In Sec. VII we will discuss this result in the context of the flux noise spectrum: a constant $|\text{Im}[1/\epsilon(\omega)]|$ corresponds to a $1/\omega$ noise.

There is also a deviation from the MP form for the unfrustrated case above the KT transition as discussed in Ref.

7: as the frequency is increased the MP form gives $|\text{Im}[1/\epsilon(\omega)]| \propto \ln(\omega)/\omega$, whereas the true behavior is a crossover to $|\text{Im}[1/\epsilon(\omega)]| \propto 1/\sqrt{\omega}$ followed by a crossover to $|\text{Im}[1/\epsilon(\omega)]| \propto 1/\omega$ for even higher frequencies. The corresponding result for the flux noise spectrum is a crossover to $1/\omega^{3/2}$ followed by $1/\omega^2$ which we will come back to in the following section.

Above the KT transition for $f=0$ there is flux flow resistance at zero frequency.² This means that the MP form cannot be valid all the way down to zero frequency because it predicts a vanishing flux flow in this limit. In the limit of very small frequencies we must come back to a conventional response of Drude type.¹³ We may phenomenologically incorporate this correction by extending the MP form into

$$\text{Re}\left[\frac{1}{\epsilon(\omega)}\right] = \frac{1}{\tilde{\epsilon}} \frac{\omega^2}{\omega^2 + \omega\omega_0 + \sigma^2}, \quad (25)$$

where $\sigma \propto \lambda^{-2}$ and λ is the screening length. The flux flow resistance R is by definition proportional to σ and according to the Coulomb gas analogy proportional to λ^{-2} . One notes that $\sigma=0$ corresponds to the pure MP case, whereas $\omega_0=0$ corresponds to the pure Drude case. In the frustrated case there is always some flux flow resistance both above and below the KT transition and in principle σ has to be finite. What we have found in our simulations is consequently that σ compared to the characteristic frequency ω_0 is very small. This is the reason for the success of the MP form. Roughly speaking the MP form suggests that the response of the bound vortex pairs dominates over the response of the free vortices. This is certainly true for our simulations for $p=2$ in a temperature region around T_c^{CG} . However, from Fig. 2 we note that in the case $p=1$ the vortex density is smaller so the density of bound pairs is smaller and hence the ratio σ/ω_0 may be expected to be larger. Figure 16 shows the unfrustrated $p=1$ case somewhat above the KT transition. This should be compared to the corresponding $p=2$ case in Fig. 5(a). The point is that the data in Fig. 16 fit much better with $\sigma/\omega_0 \approx 0.4$ than with the pure MP value $\sigma/\omega_0=0$. This is in contrast to the $p=2$ case in Fig. 5(a) where the pure MP value $\sigma/\omega_0=0$ gives a very good fit to the data. In the fitting procedure of Fig. 16 we have first obtained the imaginary part of the response function by starting from Eq. (25) and using the Kramer-Kronig relation. This leads to

$$\text{Im}\left[\frac{1}{\epsilon(\omega)}\right] = -\frac{1}{\tilde{\epsilon}} \frac{\omega\omega_0}{\pi} \frac{2\omega^2 \ln|(\omega/\sigma)| + [\omega^2 - 2(\sigma/\omega_0)^2(\omega^2 + \sigma^2)]C(\sigma/\omega_0)}{(\omega^2 + \sigma^2)^2 - (\omega\omega_0)^2}, \quad (26)$$

where

$$C(\sigma/\omega_0) = \begin{cases} \frac{1}{\sqrt{1-4(\sigma/\omega_0)^2}} \ln \left| \frac{1-\sqrt{1-4(\sigma/\omega_0)^2}}{1+\sqrt{1-4(\sigma/\omega_0)^2}} \right|, & \sigma < \omega_0/2 \\ \frac{2}{\sqrt{4(\sigma/\omega_0)^2-1}} \left[\tan^{-1} \left(\frac{1}{\sqrt{4(\sigma/\omega_0)^2-1}} \right) - (\pi/2) \right], & \sigma > \omega_0/2. \end{cases} \quad (27)$$

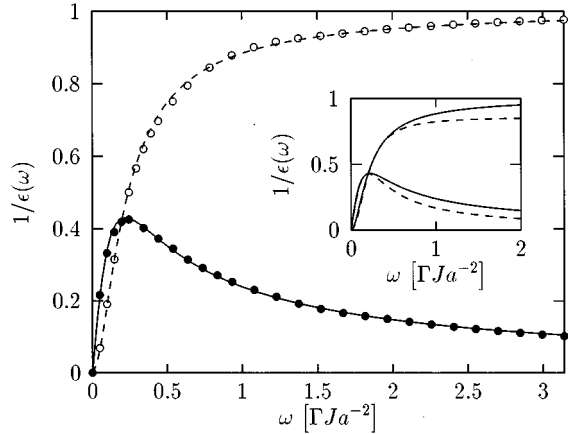


FIG. 17. The linear response function $1/\epsilon(\omega)$ as a function of ω for $p=1$ and $f=1/8$. The ratio between T_c^{CG} and T_c^{CG} is the same as in Fig. 10. The symbols are the same as in Fig. 16. The value $\sigma/\omega_0 \approx 1.5$ was obtained. Inset shows the difference between the extended MP equations and pure Drude response for this σ/ω_0 . The full lines correspond to Eqs. (25) and (26) and the dashed curves to a pure Drude response.

We have then used Eqs. (25) and (26) when fitting to the simulation data. Figure 17 illustrates the same thing for the frustrated case below the KT transition. In the case of $p=1$ the simulated data fit much better with $\sigma/\omega_0 \approx 1.5$. This should be compared to the corresponding $p=2$ case in Fig. 10 which fits very well with $\sigma/\omega_0=0$. Thus our interpretation of the difference between the $p=2$ case and the $p=1$ case is that the vortex fluctuations are dominant for the $p=2$ case which gives a vortex response close to the MP form $\sigma/\omega_0=0$, whereas for the $p=1$ case they are less dominant and this drives the vortex response towards the Drude limit $\sigma/\omega_0=\infty$.

The interplay between the MP and the Drude response behavior also manifests itself in another way. The peak ratio predicted by the MP form is $2/\pi$ (see Sec. IV). One way of measuring this peak ratio is to keep the frequency fixed and vary the temperature. The function $|\text{Im}[1/\epsilon(T_c^{\text{CG}})]|$ then has a maximum for a unique temperature. The ratio $|\text{Im}[1/\epsilon]|/|\text{Re}[1/\epsilon]|$ at this temperature is the peak ratio. Figure 18 demonstrates that this peak ratio for a certain fixed frequency is close to $2/\pi$. However, for higher frequencies the deviation from the MP form causes this ratio to increase towards 1. This is shown in Fig. 19 which shows the real and imaginary part of $1/\epsilon(\omega)$ as a function of ω for a fixed temperature T_c^{CG} . This temperature ($T_c^{\text{CG}}=2.7$) is higher than the temperature of the peak position in Fig. 18. This means that the peak in Fig. 19 corresponds to a higher frequency ω ($\omega \approx 9.4$) than the frequency in Fig. 18. At this higher frequency there is a deviation from the MP resulting in a peak ratio which is larger than $2/\pi$. The peak ratio in Fig. 19 is 0.83. The inset in Fig. 19 shows the peak ratio as a function of frequency. As seen it increases from $2/\pi$ towards 1 where the peak ratio 1 corresponds to the Drude limit. The deviation from $2/\pi$ comes because, as the temperature is increased from T_c^{CG} , more and more vortices become free and the response of the vortex pairs becomes less dominant. Another way of seeing this is to fit the data for fixed tem-

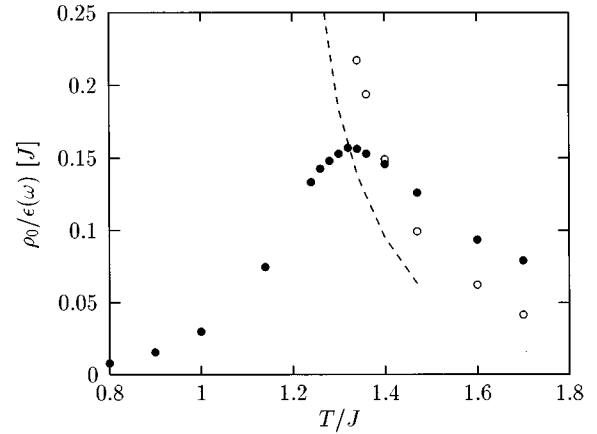


FIG. 18. Real and imaginary part of the linear response $1/\epsilon(\omega)$ as a function of temperature for fixed frequency ω . The simulation data are for $\omega=0.5$ and $p=2$. The real part $\rho_0 \text{Re}[1/\epsilon(\omega)]$ is given by the open circles and the imaginary part $\rho_0 |\text{Im}[1/\epsilon(\omega)]|$ by the filled circles. The broken curve corresponds to $(2/\pi)\rho_0 \text{Re}[1/\epsilon(\omega)]$. The broken curve cuts the imaginary part at the peak which means that the ratio between the imaginary and real part of the response at the dissipation peak is $2/\pi$, as predicted by the MP description.

perature to Eq. (25). For the high-temperature data in Fig. 19 this gives $\sigma/\omega_0 \approx 0.7$ to be compared to $\sigma/\omega_0 \approx 0$ closer to T_c^{CG} . The experimental implications of the peak ratio variation with frequency are discussed in the following section.

VII. RELATIONS TO EXPERIMENTS

In Secs. IV and V it was shown that the dynamical vortex response for our model simulations was very well described by the MP form both with and without frustration. For a superconducting film and 2D Josephson-junction array the unfrustrated case corresponds to no magnetic field applied perpendicular to the sample. It has been shown earlier that

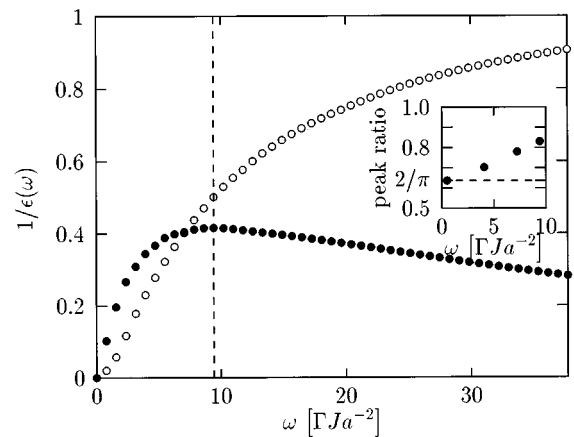


FIG. 19. The linear response function $1/\epsilon(\omega)$ as a function of ω for $T_c^{\text{CG}}=2.7 (\gg T_c^{\text{CG}})$ and $p=2$. Open circles correspond to $\text{Re}[1/\epsilon(\omega)]$ and filled circles to $|\text{Im}[1/\epsilon(\omega)]|$. The vertical dashed line denotes the frequency where $|\text{Im}[1/\epsilon(\omega)]|$ has its maximum. The peak ratio is 0.83. Inset shows the peak ratio as a function of frequency. The dashed line corresponds to $2/\pi$.

the MP form gives a good description of this case both for superconducting films^{5,7} and Josephson-junction arrays.¹⁰

The frustrated case was tested in Ref. 3. The experiments were made on 2D triangular array superconductor–normal-metal–superconductor-junctions. The complex impedance Z , which is directly related to the dielectric constant $1/\epsilon(\omega)$ was measured at a temperature below the KT transition. A rough estimate suggests that $T^{\text{CG}}/T_c^{\text{CG}} \approx 0.3$. The frustration range was up to $f \approx 0.05$. It was shown that the data were well described by the MP form. It was also shown that the data scaled as ω/f . Both these features are in precise correspondence with our simulations, as seen from Figs. 10 and 14. The fact that the simulations and experiments are in agreement suggests that the vortex characteristics obtained from the simulations are rather generic. What can then be said about the reason for this unconventional dynamical response? One argument would be to say that since $T^{\text{CG}}/T_c^{\text{CG}} \approx 0.3$ is far below the transition there are no vortex fluctuations present and consequently the response cannot in this case be caused by vortex fluctuations. This argument is countered by the present simulations: as is apparent from Fig. 2 vortex fluctuations are still present at lower temperatures and furthermore they increase as a function of frustration. This increase consists of two parts. The first is the increase of the effective temperature T^{CG} with f for fixed temperature T , as shown in Fig. 1. The second is that the density of vortex fluctuations $n-f$ increases with f for a fixed T^{CG} below T_c^{CG} as seen in Fig. 2. The simulations also gives us the possibility to manipulate the amount of vortex fluctuations by changing the p value of the model. This is illustrated by Figs. 17 and 10: as the p value is changed from 2 to 1 the dynamical response is pushed towards a more conventional Drude-type response. If vortex fluctuations were not an essential part of the cause then the difference between the $p=1$ case and the $p=2$ case for the same value of f and $T^{\text{CG}}/T_c^{\text{CG}}$ may be hard to explain. Taken together this suggests to us that the unconventional response described by the MP form is indeed linked to the vortex fluctuations also in the frustrated case below the KT transition. One may also note that, although the ω/f scaling works well both in our simulations and the experiments, the correct scaling is nevertheless ω/n where n is the vortex density as demonstrated in Figs. 11–13.

We now turn to superconducting films in a perpendicular magnetic field B . A demonstration of the ω/B scaling below the KT transition and a fair agreement with the MP form was pointed out in Ref. 2 based on data for a granular aluminum film from Ref. 17. Another striking example is given in Fig. 20. The data is for a 60-Å-thick MoGe superconducting film from Ref. 16. The data are taken at 10 kHz in a perpendicular magnetic field of 10 kOe and are plotted as a function of temperature. G is the conductance and $\omega G \propto i/\epsilon$. Consequently, the representation of the data corresponds to Fig. 18. The MP response predicts that the peak ratio should be $2/\pi$. To check this we have plotted $(2/\pi)\omega\text{Im}[G]$ (dashed line). As seen in Fig. 20 it cuts the $\omega\text{Re}[G]$ data precisely at the peak. According to our simulations this suggests that the response is due to vortex fluctuations. Although the $2/\pi$ ratio is a irrefutable feature of the data, one can of course argue about the cause. In Ref. 16 the data in Fig. 20 are attributed

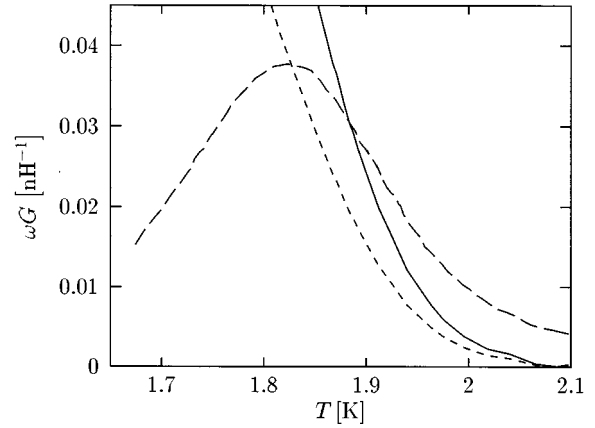


FIG. 20. Real and imaginary parts of ωG for a 60-Å MoGe superconducting film measured in a field of 10 kOe and a frequency of 10 kHz. The experimental data is taken from Ref. 16. The full, long dashed, and short dashed curves correspond to $\omega\text{Im}[G]$, $\omega\text{Re}[G]$, and $(2/\pi)\omega\text{Im}[G]$, respectively. This demonstrates that the peak ratio is $2/\pi$ to very good approximation.

to pinning. However, the peak ratio together with the present simulations point in a different direction: the rather high magnetic field (in relation to H_{c2}) induces enough vortex fluctuations to cause a MP response. This type of vortex fluctuations can then in principle be dominating all the way down to the melting of the vortex lattice.

We now turn to possible experimental consequences of the deviations from the MP form found in the simulations which were discussed in Sec. VI. We found that for the unfrustrated case above, but very close to, the KT transition the function $|\text{Im}[1/\epsilon(\omega)]|$ is fairly constant over an extended frequency interval $0 < \omega < \omega_{\text{max}}$ (compare discussion in connection with Fig. 15). According to Ref. 7 the relation to the flux noise spectrum is

$$S_{\Phi}(\omega) = \frac{4\pi T^{\text{CG}}}{\omega} \left| \text{Im} \left[\frac{1}{\epsilon(\omega)} \right] \right|, \quad (28)$$

where Eq. (28) is valid to the extent that the effects associated with the boundary of the flux noise measuring region play a minor role. Equation (28) together with the fact that $|\text{Im}[1/\epsilon(\omega)]|$ is constant over an extended frequency interval $0 < \omega < \omega_{\text{max}}$ predicts that $S_{\Phi}(\omega)$ is proportional to $1/\omega$. Such a $1/\omega$ flux noise has been measured in Ref. 4 in case of a 2D square lattice Josephson-junction array. Of course the fact that the $1/\omega$ noise is a property both of the simulations and the measurements does not necessarily mean that the cause is the same. In the simulations there is always an ω_{cut} . For frequencies larger than this upper limit $S(\omega)$ crosses over to $S(\omega) \propto \omega^{-3/2}$. According to the simulations this cutoff frequency should be rather independent of temperature (compare Fig. 15). The data of Ref. 4 do not show any such cutoff. However, this might just mean that this cutoff frequency is beyond the frequency range of the experimental setup in Ref. 4. Other flux noise measurements such as the one on $\text{Bi}_2\text{Sr}_2\text{CaCu}_2\text{O}_8$ films in Ref. 5 definitely have such a crossover at higher frequencies,^{5,7} as well as agreement with the MP form. To the extent that Eq. (28) is valid there has to exist such a cutoff because the response function

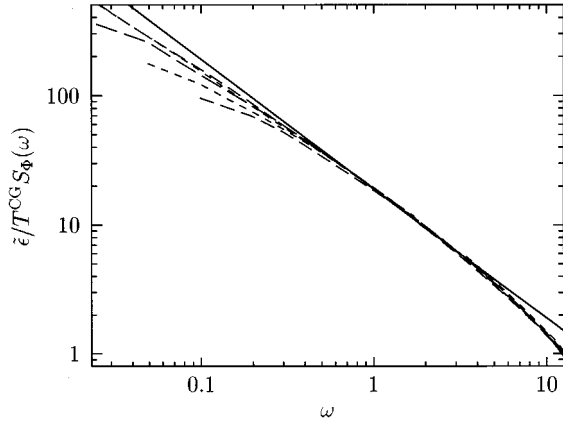


FIG. 21. $\bar{\epsilon}/T^{\text{CG}}S_{\Phi}(\omega)$ as a function of ω for five temperatures above T_c . The upper short dashed, upper medium dashed, long dashed, lower short dashed, and lower medium dashed curves correspond to $T^{\text{CG}}/T_c^{\text{CG}} \approx 1.1, 1.3, 1.4, 1.6,$ and 1.75 , respectively. The full line has slope -1 which corresponds to a $1/\omega$ noise.

$|\text{Im}[1/\epsilon(\omega)]|$ has to vanish in the high-frequency limit. The flux noise data in Ref. 4 were found to obey a scaling function $\omega S_{\Phi}(\omega/\omega_0)$. According to Eq. (28) this means that $|\text{Im}[1/\epsilon(\omega)]|$ is only a function of ω/ω_0 , where ω_0 is a characteristic frequency. This is also the scaling idea behind the MP form. However, there is one difference between the scaling form found in the experimental data and the implications of Eq. (28): comparison between Eqs. (28) and (16) shows that the amplitude of $\omega S_{\Phi}(\omega/\omega_0)$ as a function of temperature is proportional to $T^{\text{CG}}/\bar{\epsilon}$. Thus the scaling in the experimental data and the simulations are consistent to the extent that $T^{\text{CG}}/\bar{\epsilon}$ is almost constant for the experimental data presented in Ref. 4. This is quite possible because according to the simulations the $1/\omega$ noise only shows up in a very narrow T^{CG} region above T^{CG} . In Fig. 21 we have plotted $\bar{\epsilon}/T^{\text{CG}}S_{\Phi}(\omega)$ versus ω in logarithmic scales as obtained from our simulations. The full line in Fig. 21 has slope -1 and corresponds to a $1/\omega$ noise. The agreement with Fig. 2 in Ref. 4 is indeed striking. However, the simulation data in Fig. 21 have a large frequency cutoff beyond which the data fall below the $1/\omega$ line. The experimental data in Fig. 2 of Ref. 4 show no such deviation from this line. In order to further investigate the connection between the experimental flux noise data and our simulations it would be helpful to also have the experimentally measured complex impedance. For example, a break down of Eq. (28) would immediately suggest that other effects beyond the “pure” vortex fluctuations extracted from our present simulations come into play.

As discussed in Sec. VII there was the crossover towards a Drude response behavior as the temperature was increased. As a consequence the peak-ratio $|\text{Im}[1/\epsilon]|/\text{Re}[1/\epsilon]$ should increase from $2/\pi$ towards 1 as the frequency is increased. This effect was illustrated in Fig. 18. In Fig. 22 we give the peak ratios for a 30-Å-thick MoGe superconducting film measured in Ref. 18. The conductance G was obtained in zero perpendicular magnetic field as a function of temperature for three different frequencies 1, 10, and 100 (kHz), respectively. Just as in the case of our simulations the experimental data increases from the MP value $2/\pi$ for small frequencies towards 1 at higher frequencies.

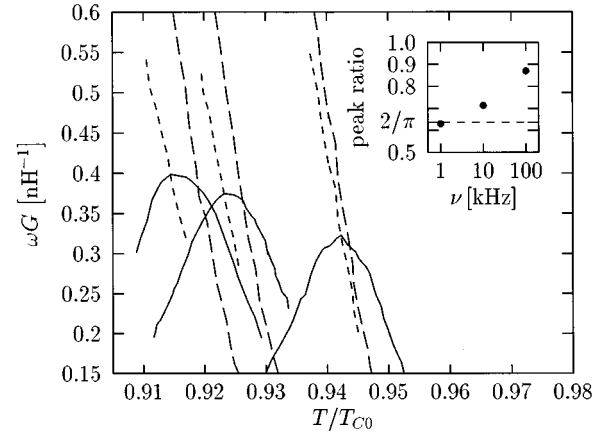


FIG. 22. Real and imaginary part of ωG for a 30-Å MoGe superconducting film measured at three different frequencies ν . The experimental data is taken from Ref. 18. The curves shows from left to right data for $\nu=1, 10,$ and 100 kHz, respectively. The long dashed curves correspond to the imaginary part and the full curves to the real part of ωG . The short dashed curves show $C\omega\text{Im}[G]$ where the constant C has been adjusted so that the short dashed curves pass through the maximums of $\omega\text{Re}[G]$. Consequently, C is the peak ratio. The inset shows the peak ratios determined in this way for the three frequencies.

VIII. CONCLUDING REMARKS

In the present paper we have presented results from our extensive simulation of the 2D XY -type models with TDGL dynamics. We have tried to demonstrate that when interpreted in terms of effective vortex variables the simulation results can be turned into a cogent picture. The results are then described in terms of vortex density, effective vortex temperature, screening length, dielectric constant, frustration, and so forth. The dynamical properties were to a large extent found to be described by the MP response function and a characteristic frequency ω_0 . We have found that the MP response describes the dynamics both above and below the KT transition and furthermore also the case with frustration. We have investigated how the characteristic frequency ω_0 depends on the other effective vortex variables and have also been able to extract a critical behavior for ω_0 at the KT transition.

An interesting question is then how generic these simulation results for 2D vortex dynamics really are. Here the circumstantial evidence indicates that the results could be quite generic: for the unfrustrated case above the KT transition it has been shown that the MP response function describes the experimental data very well.^{5,10} The deviations from the MP response found in the simulations also seem to have a direct correspondence in the experiments as discussed in connection with Fig. 22. In the unfrustrated case below the KT transition simulations for a 2D Coulomb gas with Langevin dynamics show good agreement with the MP response.⁹ This suggests that the MP response is indeed linked to the vortex degrees of freedom because the vortex system maps onto the 2D Coulomb gas system.² For the frustrated case it has been shown that the MP response describes a frustrated Josephson-junction array very well.³ We have here shown that a frustrated XY model with TDGL dynamics is similarly described by the MP response.

The picture which emerges from the simulations suggests that the MP response is linked to the density of vortex fluctuations. In a rough sense the MP response can be viewed as the response due to the vortex pairs. The deviations from the MP response found in the simulations can be understood from such an assumption. A particularly interesting thing was that the simulations indicated that the MP response in the frustrated case was valid far below the KT transition temperature of the unfrustrated case. Again measurements point in the same direction as shown in Fig. 20 and in Ref. 3.

The simulations also indicated the existence of an approximate $1/\omega$ noise in the flux noise spectrum. However, whether or not this $1/\omega$ noise can be linked to the measured $1/\omega$ noise in Ref. 4 is at present an open question.

A deeper theoretical understanding of the properties of 2D vortex dynamics, which have emerged from our simula-

tions, is lacking at present. However, we hope that the critical behavior of the characteristic frequency and the various scaling relations which we have extracted from our simulations will serve as helpful clues. Another input, which might lead to further understanding, would be experiments designed to test how generic the results found in the present paper are.

ACKNOWLEDGMENTS

Stimulating discussions with and a critical reading of the manuscript by Peter Olsson are gratefully acknowledged. This work was supported by the Swedish Natural Research Council through Contract Nos. F-FU 04040-322 and E-EG 04040-327.

-
- ¹J. M. Kosterlitz and D. J. Thouless, *J. Phys. C* **5**, L124 (1972); **6**, 1181 (1973); V. L. Berezinskii, *Zh. Eksp. Teor. Fiz.* **61**, 1144 (1972) [*Sov. Phys. JETP* **34**, 610 (1972)].
- ²For a review see, e.g., P. Minnhagen, *Rev. Mod. Phys.* **59**, 1001 (1987).
- ³R. Théron, J.-B. Simond, Ch. Leeman, H. Beck, P. Martinoli, and P. Minnhagen, *Phys. Rev. Lett.* **71**, 1246 (1993).
- ⁴T. J. Shaw, M. J. Ferrari, L. L. Sohn, D.-L. Lee, M. Tinkham, and J. Clark, *Phys. Rev. Lett.* **76**, 2551 (1996).
- ⁵C. T. Rogers, K. E. Myers, J. N. Eckstein, and I. Bozovic, *Phys. Rev. Lett.* **69**, 160 (1992).
- ⁶P. Martinoli, P. Lech, Ch. Leeman, and H. Beck, *Jpn. J. Appl. Phys.* **26**, Suppl. 26-3, 1999 (1987).
- ⁷J. Houlrik, A. Jonsson, and P. Minnhagen, *Phys. Rev. B* **50**, 3953 (1994).
- ⁸For a review see, e.g., S. R. Shenoy, *Lecture Notes on Josephson Junctions Arrays* (Troisième Cycle de la Physique, Neuchâtel and Lausanne, 1989).
- ⁹K. Holmlund and P. Minnhagen, *Phys. Rev. B* **54**, 523 (1996).
- ¹⁰M. Wallin, *Phys. Rev. B* **41**, 6575 (1990).
- ¹¹E. Domani, M. Schick, and R. Swendsen, *Phys. Rev. Lett.* **52**, 1535 (1984).
- ¹²A. Jonsson, P. Minnhagen, and M. Nylén, *Phys. Rev. Lett.* **70**, 1327 (1993).
- ¹³P. Minnhagen and O. Westman, *Physica C* **220**, 347 (1994).
- ¹⁴P. Olsson, *Phys. Rev. B* **46**, 14 598 (1992); Ph.D. thesis, Umeå University, 1992.
- ¹⁵Note that this Coulomb gas particle definition of the vortex density differs slightly from the vortex density obtained directly from the phase difference around an elementary square; see Ref. 14.
- ¹⁶A. Kapitulnik, A. Yazdani, J. S. Urbach, W. R. White, and M. R. Beasley, *Physica B* **197**, 530 (1994).
- ¹⁷A. T. Fiory and A. F. Hebard, *Phys. Rev. B* **25**, 2073 (1982).
- ¹⁸A. Yazdani, Ph.D. thesis, Stanford University, 1994.